JOURNAL OF GEOPHYSICAL RESEARCH, VOL. 118, 1–12, doi:10.1029/2012JA018275, 2013

Spatial distributions of ion pitch angle anisotropy in the near-Earth magnetosphere and tail plasma sheet

Chih-Ping Wang,[1] Sorin G. Zaharia,[2] Larry R. Lyons,[1] and Vassilis Angelopoulos[3]

Received 7 September 2012; accepted 16 November 2012.

[1] We have quantified anisotropy of ion pitch angle distributions observed by the Time History of Events and Macroscale Interactions during Substorms (THEMIS) spacecraft and determined statistically how anisotropy varies with particle energy, as well as spatial distributions and dependences on geomagnetic activity. In the tail plasma sheet, ions from a few keV to a few tens of keV are mostly isotropic. The locations and energy ranges for these isotropic ions and their changes with *Dst* are consistent with ions being isotropized by current sheet scattering predicted using empirical magnetic field models. Ions of a few hundreds of keV in the tail have cigar-shaped or unidirectional pitch angle distribution (PAD) and are likely a result of Speiser motion. The majority of ions in the near-Earth magnetosphere are expected to conserve their first and second adiabatic invariants as they move with pitch angle dependent drift. This gives drift shell splitting, which plays an important role in generating pancake-shaped PAD observed from ~1 keV up to hundreds of keV. The magnetic local time of the pancake PAD rotates with increasing energy. Loss of near 90° ions due to magnetopause shadowing can further explain the butterfly-shaped PAD observed at the postmidnight sector at energies above 30 keV. For ions below a few hundreds of eV in the tail plasma sheet and the near-Earth magnetosphere, their PAD is dominantly bidirectional, which is likely due to ionosphere outflow. High-energy ions on the dayside become less anisotropic during higher *AE*, when pitch angle scattering by electromagnetic ion cyclotron waves may play an important role.

Citation: Wang, C.-P., S. G. Zaharia, L. R. Lyons, and V. Angelopoulos (2012), Spatial distributions of ion pitch angle anisotropy in the near-Earth magnetosphere and tail plasma sheet, *J. Geophys. Res.*, *118*, 1–12, doi:10.1029/2012JA018275.

1. Introduction

[2] There are many processes that can alter ion pitch angle distributions (PADs), including particle motion, magnetic field configuration, pitch angle dependent sources and losses, and wave-particle interactions. Change of pitch angle can lead to particle precipitation to the ionosphere and formation of aurora. Some particular pitch angle distribution can allow for growth of waves, such as the electromagnetic ion cyclotron (EMIC) waves. Changes in PADs also affect pressure anisotropy, which is important to plasma and magnetic field structures and instabilities. In this study we quantify the anisotropy of ion PADs observed by the Time History of Events and Macroscale Interactions during Substorms (THEMIS) spacecraft to statistically determine how anisotropy varies with particle energy, equatorial location, and geomagnetic activity. We then evaluate whether the observed anisotropy can be accounted for by any of the above processes.

[3] Ion motion can vary from being adiabatic (conserving the first or second adiabatic invariants) to being chaotic or being Speiser-type [e.g., *Speiser*, 1965] depending on the particle gyroradius relative to the curvature radius of background magnetic field [e.g., *Sergeev et al.*, 1983]. The chaotic motion can cause pitch angle diffusion, leading to isotropic PADs. A Speiser-type trajectory includes meandering motion at the center of magnetic field reversal and escaping and returning to the reversal along a more field-aligned direction. Under adiabatic motion, particles of the same energy but with different pitch angles drift differently in magnetic local time (MLT)-dependent electric and magnetic field, resulting in more particles within one pitch angle range than the others [e.g., *Roederer et al.*, 1973]. The difference in drift paths can also lead to more loss of near 90° particles to the magnetopause compared to more field-aligned particles. In the inner magnetosphere near the geocorona, particle loss due to charge exchange is quicker for field-aligned particles than those of other pitch angles because of their lower mirror altitudes [e.g., *Fok et al.*, 1991]. Ion outflows are mainly field-aligned, thus enhancing the number of particles at pitch angles around 0° and 180°. Waves can also break

[1]Department of Atmospheric and Oceanic Sciences, University of California, Los Angeles, California, USA.
[2]Space Science and Applications (ISR-1), Los Alamos National Laboratory, Los Alamos, New Mexico, USA.
[3]Department of Earth and Space Sciences, University of California, Los Angeles, California, USA.

Corresponding author: C.-P. Wang, Department of Atmospheric and Oceanic Sciences, University of California, Los Angeles, California, USA. (cat@atmos.ucla.edu)

0148-0227/13/10.1029/2012JA018275

conservation of particle first and second adiabatic invariants, causing pitch angle diffusion [e.g., *Jordanova et al*., 2001].

[4] Previous observational studies have shown that ion anisotropy varies significantly with particle energy, location, and geomagnetic activity. For example in the near-Earth region, *Nagai et al*. [1983] using ISEE-1 and *Chappell et al*. [2008] using Polar found that magnetospheric ions below several hundreds of eV at $L < 10$ are often bidirectional on the dayside and unidirectional on the nightside, likely resulting from contribution of ions from the ionosphere. *Fritz et al*. [2003] showed butterfly PADs for ions > 20 keV on the nightside from $r = 6$ to 12 R_E observed by ISEE-1, which can be explained by drift shell splitting combined with magnetopause shadowing. Using AMPTE/CCE, *Sibeck et al*. [1987] showed that PADs with larger fluxes near 90° for 34–50 keV ions dominate the entire dayside magnetosphere at $r < \sim 9$ R_E, also due to drift-shell splitting. Using AMPTE/CCE, *Takahashi et al*. [1997] showed that substorm injection changes the nightside radial profiles of particle fluxes and, as these particles drift to the dayside along pitch angle dependent drift shell, results in changes in the anisotropy of PADs on the dayside. *Fennell et al*. [1981] investigated P78-2 satellite data and found that ion PADs at $r = 5.3$ to 7.8 R_E change from being predominantly field aligned at lower energy (< a few keV) to being peaked perpendicular to magnetic field at higher energy. Compared to the near-Earth magnetosphere, only limited studies have been conducted for ion anisotropy in the tail plasma sheet. *Walsh et al*. [2011] showed that ions observed by Cluster in the magnetotail central plasma sheet at $r \sim 19$ R_E are isotropic from a few hundreds of eV to 40 keV, likely due to current sheet scattering, but ions below a few hundreds of eV have higher fluxes in the field-aligned direction, likely due to ionospheric outflow. *Sergeev et al*. [1993] showed high-energy ions change from being isotropic in the tail plasma sheet to anisotropic at $r \sim 5$–9 R_E, where the magnetic field lines become not stretched enough to cause pitch angle scattering. Nevertheless, the above studies only cover limited ion energy ranges and spatial locations. Furthermore, there is only limited understanding of the dependence of the ion anisotropy on geomagnetic activity.

[5] In this study we used THEMIS measurements from 2007 to 2010 to statistically determine the spatial distributions of ion anisotropy at different energies with much wider spatial ranges ($r = 7$ to 20 R_E) and energy ranges (0.05 to 600 keV) than the previous studies discussed above. As described in section 2, THEMIS has measured plasma in the magnetosphere at low latitudes since 2007, providing sufficient data coverage for establishing spatial distributions with a good spatial resolution. In section 3, we describe how the ion anisotropy changes with particle energy, radial distance and MLT, and *Dst*. In section 4, we investigate if any of the previously proposed processes plays a dominant role in causing the observed anisotropy.

2. Data Selection

[6] In this study, we used measurements from the five THEMIS spacecraft (TH-A, B, C, D, and E) from 1 December 2007 to 30 April 2010. Aberrated GSM coordinates (with the aberration angle determined by 1 h averaged solar wind velocity) are used. THEMIS spacecraft move in low latitude orbits. During our selected period, TH-A, D, and E covered regions inside $r \sim 12$ R_E while TH-B and C covered regions inside $r \sim 30$ R_E.

[7] Ions and electrons are measured by an electrostatic analyzer (ESA, 0.006–20 keV/q for ions and 0.007–26 keV for electrons [*McFadden et al*., 2008]) and a solid state telescope (SST, 35 keV–6 MeV for ions and 30 keV–6 MeV for electrons). Full distributions are used with time resolution of a few minutes. For the SST data prior to December 2007, the current calibration factors are unreliable due to an extended commissioning phase of the SST instruments. We thus only used data after December 2007. For each measured energy spectrum, contamination to ESA and SST is removed. The penetrating radiation contamination is removed from the ESA data by subtracting the minimum count value within the ESA energy ranges (see Appendix of *Wang et al*. [2011] for details). The sunlight contamination to the SST is removed (defined by a criteria that considers a data point being contaminated if its modified z-score calculated across azimuthal angle is greater than 3.5. The modified z-score is a normalized outlier detection test [*Iglewicz and Hoaglin*, 1993]. For a data point with value x_i, its modified z-score is $0.6745 \cdot (x_i - x_{\text{median}})/\text{median}(|x_i - x_{\text{median}}|)$. However, there is no reliable method to remove the penetrating radiation contamination to the SST. Therefore, in this study we restricted the region to $r \geq 7$ R_E, where there is little radiation contamination. The 3D particle fluxes in field-aligned coordinates are sorted into eight pitch angle channels (the center of each channel is at 11.25°, 33.75°, 56.25°, 78.75°, 101.25°, 123.75°, 146.25°, 168.75°), with the flux within each pitch angle channel being averaged over the azimuthal direction. For ions, there is an energy gap (from ~20 to 28 keV) between the highest ESA channel and the lowest SST channel. We interpolate the fluxes for this energy gap using the fluxes from the two nearby energy channels.

[8] We identified each THEMIS crossing of the bow shock and magnetopause and sorted each measurement into the region of the magnetosheath and magnetosphere. Inside the magnetosphere, we included only data within the plasma sheet using a β criterion. The plasma sheet is centered at the equatorial plane. Central plasma sheet crossings are selected when plasma β (defined as $(P_{\text{ion}} + P_{\text{electron}})/(B^2/(2\mu_0))$ satisfies the criteria: $\beta \geq 1$, for $r \geq 15$ R_E and $\beta \geq 10^{0.14r-2.1}$ for $r < 15$ R_E. The β criteria is r dependent since β in the equatorial plane decreases with decreasing r. Since a PAD can be changed simply due to large ion drift speed shifting a distribution in the $V_\perp$ and $V_\parallel$ plane, we only selected data with ion bulk velocity $|V| \leq 50$ km/s (the thermal speed of 13 eV ions is ~50 km/s) in the plasma sheet.

[9] Historically, PADs of different shapes are given specific names. A PAD with a peak at 90° is called 'pancake', while a PAD with peaks at 0° and 180° is called 'cigar' or 'bidirectional' [*Baker et al*., 1978] and a PAD with peaks at 0° (or 180°) is 'unidirectional'. A 'butterfly' distribution is for a PAD that is relatively depleted at 0° and 90° [*West et al*., 1973]. In this paper, we did not identify each PAD with one of the shapes described above. We quantify a

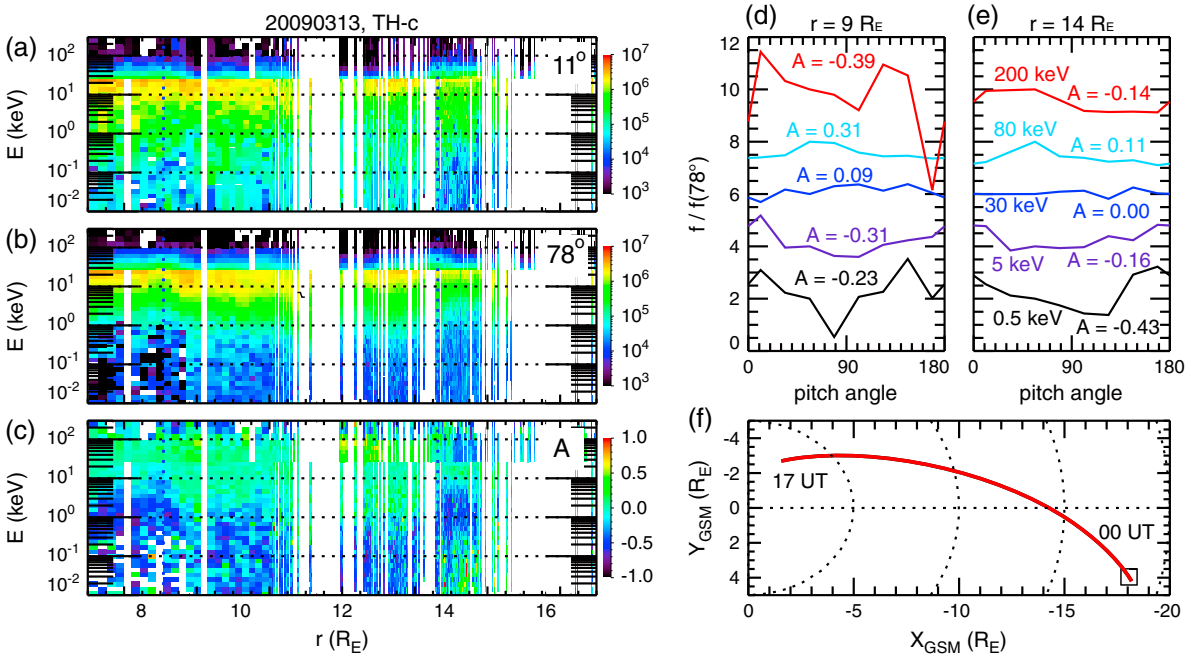

Figure 1. Energy spectrum of ion energy fluxes (1/s-sr-cm^2) at (a) 11° and (b) 78° pitch angles and of (c) ion anisotropy observed by THEMIS-C on 13 March 2009 (only data that satisfy our plasma sheet criteria were plotted). The pitch angle distributions of phase space density at different energies (0.5, 5, 30, 80, and 200 keV) and their anisotropy observed at (d) $r \sim 9$ R_E (at ~13:58 UT) and (e) $r \sim 14$ R_E (at ~09:01 UT) as indicated by the two vertical dotted lines shown in (a) to (c). The phase space density profile for each selected energy is normalized to that of 78° and is shifted arbitrarily in the *Y*-axis for better viewing. (f) The *X*-*Y* projection of THEMIS-C trajectory from 00–17 UT.

PAD for each energy channel with its anisotropy using the definition given by *Chen et al.* [1998],

$$A \equiv \frac{\int_0^{\pi/2} f(\alpha_0)\sin^3\alpha_0 d\alpha_0}{\int_0^{\pi/2} f(\alpha_0)\cos^2\alpha_0 \sin\alpha_0 d\alpha_0} - 1$$

where α_0 is equatorial pitch angle ($A = 0$ corresponding to pitch angles isotropy at that energy). Positive (negative) A indicates larger (smaller) fluxes near the 90° relative to other pitch angles. A pancake PAD has positive A, while a cigar PAD has negative A.

[10] Figure 1 shows an example of ion energy fluxes at 11° and 78° pitch angles and anisotropy as a function of particle energy observed by THEMIS-C on 13 March 2009 as the spacecraft moved earthward from the plasma sheet to the inner magnetosphere at near midnight MLTs. The PADs at selected energies at different radial distance are shown in Figures 1d and 1e. It can be seen that the ion anisotropy varies significantly with particle energy and with location. To determine statistically the variations, we computed spatial distributions of anisotropy by sorting the selected data into either 1 R_E × 1 R_E *X*-*Y* bins or 2 h × 0.25 R_E MLT-*r* bins. To determine the dependence of anisotropy on geomagnetic activity, we have investigated the changes of anisotropy with *Dst* and *AE*. As discussed in section 4.1, we evaluated the importance of current sheet scattering on isotropizing ions using the Tsyganenko 96 and 01 magnetic field models and *Dst* is one of the input parameters for the models. Therefore, in this paper we present mainly the activity dependence on *Dst* so that we can compare the model evaluations with the observed results more appropriately. We sorted the data into three different *Dst* levels: (1) weak: $10 > Dst > -5$ nT, (2) moderate: $-5 > Dst > -20$ nT, and (3) strong: $-20 > Dst > -100$ nT. Within each bin, the 25%, 50% (median), and 75% quartiles are computed.

3. Statistical Distributions of Ion Anisotropy

[11] The equatorial distributions of the median A for 11 selected ion energies (0.05, 0.1, 0.5, 1, 5, 10, 20, 45, 70, 100, and 200 keV) for the three different *Dst* levels are shown in Figure 2. The distributions of A as a function of ion energy along the noon, dusk, midnight, and dawn MLT are shown in Figure 3a, and the radial profiles of A for 5 selected energies (0.5, 5, 20, 70, and 200 keV) at the four MLTs are shown in Figure 3b. At the weak *Dst* level, in the tail plasma sheet (defined here as the nightside region at $r \geq 10$ R_E), A for ions from several hundreds of eV up to ~20 keV is nearly isotropic, but moderately negative A is seen for the majority of ions above ~200 keV and below ~0.1 keV. For ions between ~20 and 200 keV, A is dominantly isotropic in the premidnight sector and positive A can also be seen sometimes near midnight. In the postmidnight sector, a horn-shape region of negative A is seen near the dawn-flank magnetopause tailward of $X = 0$ (as indicated by the black curves in the 20 keV plot of Figure 2a), and for higher energies it extends westward into the midnight MLT at $r < 10$ R_E.

[12] In the near-Earth magnetosphere (defined here as the region from $r \leq 10$ R_E on the nightside and the whole dayside magnetosphere), A for ions below a few hundreds of eV is

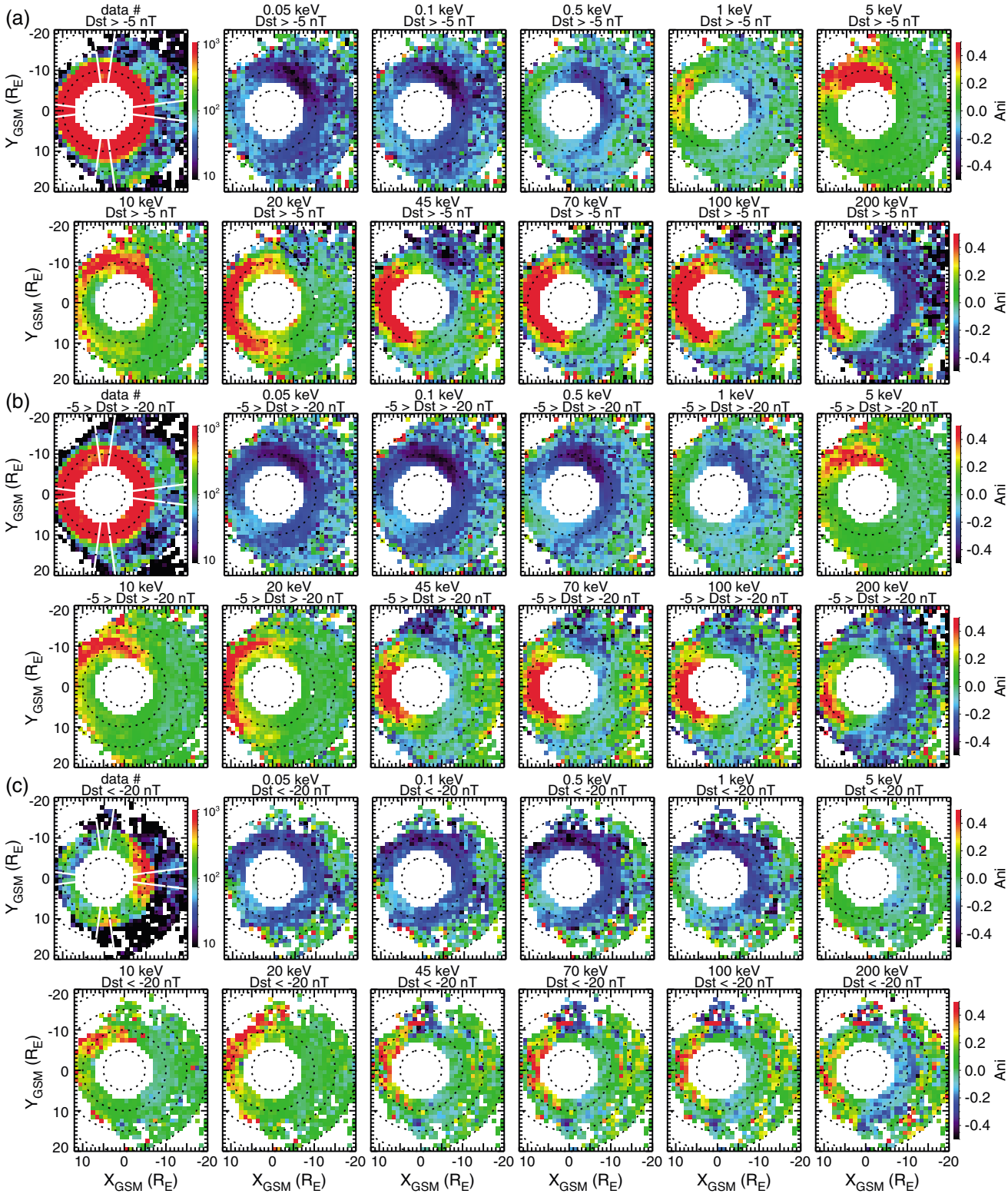

Figure 2. The equatorial distributions of number of measurements and median ion anisotropy at different energies at (a) $Dst > -5$ nT, (b) $-5 > Dst > -20$ nT, and (c) $Dst < -20$ nT. The black dashed curves in the 20 keV plot of Figure 2a indicate the horn-shape region.

slightly negative on the dayside but is strongly negative on the nightside, especially in the postmidnight sector. As ion energy increases to above 1 keV, the overall A gradually becomes positive. As shown in Figure 2, at 1 keV, a region of strongly positive A is seen at $r \sim 10\ R_E$ at the prenoon MLTs. As ion energy increases from 1 to 10 keV, this region rotates westward as well as moves toward smaller r, reaching the midnight MLT and $r \sim 7\ R_E$ at 10 keV. As the region

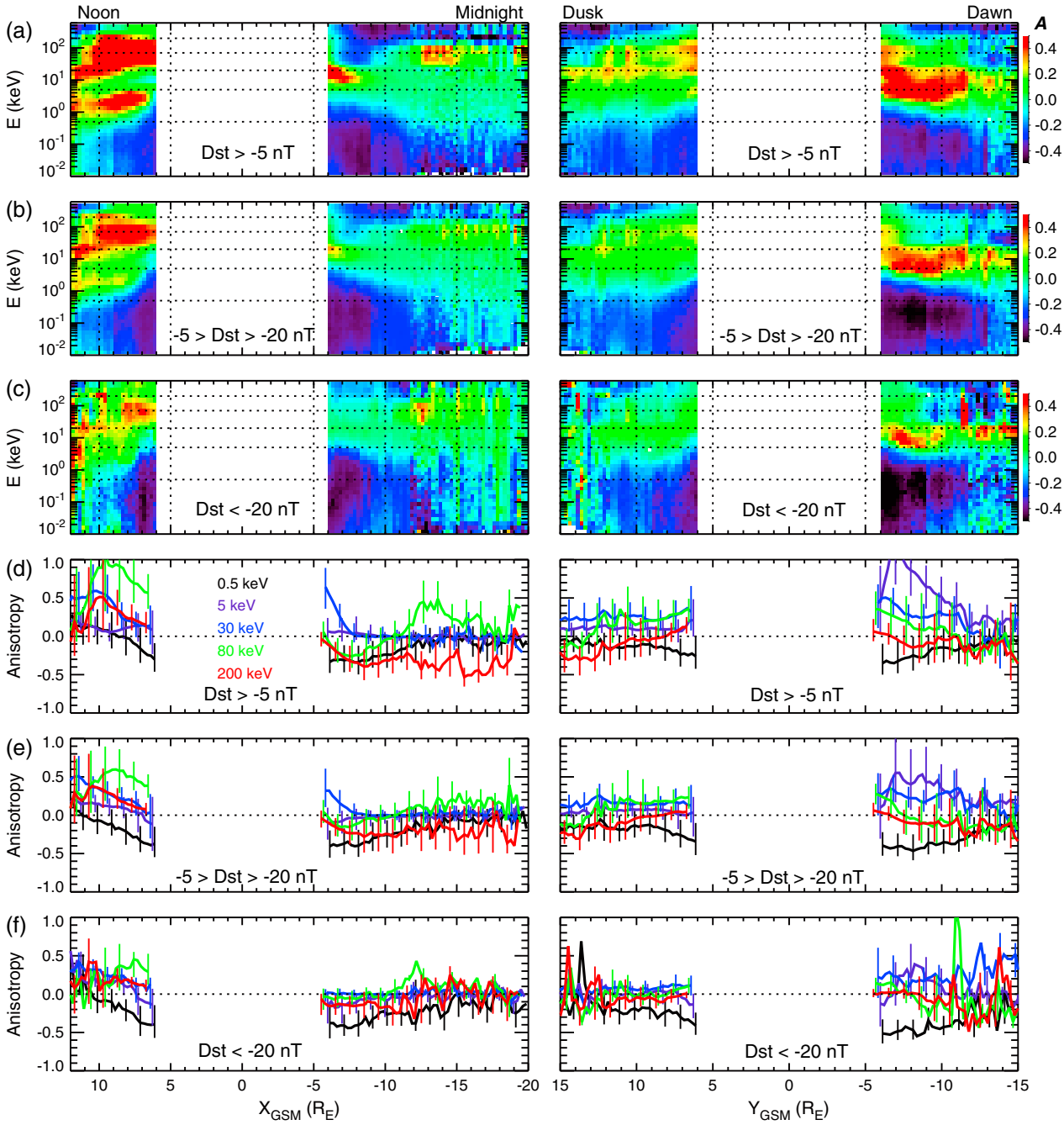

Figure 3. The median ion anisotropy versus ion energy along different MLT medians indicated by the white lines in Figure 2 at (a) $Dst > -5$ nT, (b) $-5 > Dst > -20$ nT, (c) $Dst < -20$ nT. The radial profiles of median ion anisotropy (unless otherwise indicated, the curves in the figures of this paper for statistical results show median values while the vertical lines indicate the ranges of 25% and 75% percentiles) at selected ion energies along different MLT medians at (d) $Dst > -5$ nT, (e) $-5 > Dst > -20$ nT, (f) $Dst < -20$ nT.

rotates, the peak value within it becomes smaller. At ~10 keV, a second region of strongly positive A forms at almost all the dayside MLTs at $r > 10\ R_E$. With increasing energy to several tens of keV, this second region moves inward and its dayside MLT extent becomes narrower, while the first region of strongly positive A continues to weaken and eventually becomes negative when energy is above ~30 keV. This negative region seen at >~30 keV at around midnight appears to be connected with the postmidnight horn-shape negative A region in the tail plasma sheet described above. This day-night asymmetry with positive A on the dayside and negative A on the nightside persists as energy increases to several hundreds of keV, while $|A|$ in the positive (negative) region gradually becomes smaller (larger).

[13] The change of A with the Dst levels varies with ion energy. As the Dst level changes from weak to strong, the negative A seen at ions below ~0.1 keV changes little in the near-Earth magnetosphere but becomes less negative in

the tail plasma sheet. For ions from 0.1 to several keV (see the 0.5 and 1 keV shown in Figure 2), the region of negative A extends from being on the nightside $<\sim 10\ R_E$ at the weak *Dst* level to both the dayside and the tail plasma sheet at stronger *Dst* levels. Figure 3a shows that when the *Dst* level is weak, in the tail plasma sheet there is clear separation of anisotropy at ~0.1 to 0.5 keV with negative A seen at <0.1 keV and isotropic A at >0.5 keV. However, this separation becomes less definite at stronger *Dst* levels when isotropic A occurs more often at <0.1 keV and negative A more often at 1 to 5 keV. For ions above ~10 keV, regardless of having positive A, such as that seen on the dayside, or having negative A, such as that in the horn-shape region and that in the tail at ions >200 keV, the sign of A remains with strengthening *Dst* level but the overall $|A|$ is found to become substantially smaller, that is, PAD changes toward being less anisotropic.

[14] In the next sections, we discuss different processes that can result in the observed anisotropy at different energies and regions.

4. Processes Affecting the Ion Anisotropy

[15] As ions gyrate around the magnetic field and bounce along the magnetic field line, many processes can change a PAD. The gyro and bounce motions can be adiabatic or be altered by nonadiabatic processes. Under adiabatic motion, a PAD can be affected by any process that depends on pitch angle, such as drift motion, and particle sources or losses. Nonadiabatic processes, such as current sheet scattering and wave-particle interaction, can result in pitch angle diffusion that isotropizes ions.

4.1. Particle Motion

[16] If magnetic field changes sharply on a scale smaller than a particle gyroradius, then the particle first and second invariants will no longer be conserved, which can result in stochastic particle motion leading to pitch angle scattering. This can occur near the current sheet where the magnetic field curves sharply as B_x or B_y changes direction or for high-energy particles that have large gyroradius. There have been many studies [e.g., *Sergeev et al*., 1983; *Burkhart and Chen*, 1991; *Büchner and Zelenyi*; 1989; *Delcourt et al*., 1996; *Young et al*., 1999] on how the particle motion and the resulting PAD change with the ratio of magnetic field line curvature to gyroradius, $K = R_c/\rho$, where $R_c = B_z/(\partial B_{xy}/\partial z)$ is the field line curvature radius at the equator and $B_{xy}^2 = (B_x^2 + B_y^2)$, and $\rho = mV/eB_z$ is the gyroradius for a particle of mass m, charge e, and velocity V. K is smaller when the particle energy is higher or when the magnetic field is more stretched. It is found that particles with $K > \sim 8$ can conserve their adiabaticity. (Note that $K = 8$ is an estimate given by *Sergeev et al*. [1983]; estimates in the other studies mentioned above are similar, though slightly different). For particles with $K \leq \sim 8$, their motion becomes more chaotic with decreasing K and the resulting pitch angle scattering becomes more efficient in isotropizing PAD. When $K \ll 1$, some particles may experience transient Speiser-type motion [e.g., *Burkhart and Chen*, 1991; *Buchner and Zelenyi*, 1989].

[17] To evaluate K for ions of different energies, we used three magnetic field models: (1) the Tsyganenko 96 (T96) model [*Tsyganenko*, 1995, 1996], (2) the Tsyganenko 02 (T02, also known as T01) model [*Tsyganenko*, 2002a, 2002b], and (3) Model 3: T96-based magnetic field with modification. For each THEMIS measurement we computed B_z and $\partial B_x/\partial z$ at $(x, y, z = 0)$ assuming no dipole tilt and using observed *Dst*, solar wind dynamic pressure, IMF By, and IMF Bz (additional G1 and G2 inputs for the T02 model for parameterizing 1 h solar wind history) at the time as inputs for the models. Comparing the T96 field with the observations statistically show that T96 B_z greatly underestimates the observed B_z in the tail while it overestimates the observed B_z around the dawn and dusk MLTs [e.g., *McCollough et al*., 2008]. The T96 field also has a limitation of being dawn-dusk symmetric. On the other hand, with newer methods of modeling external currents, the T02 gives better prediction in the inner magnetosphere than does the T96 and is capable of reproducing observed dawn-dusk asymmetry [e.g., *Huang et al*., 2008, *Zhang et al*., 2010], but it is limited to only give reliable magnetic field inside $r = 15\ R_E$. Because of these large uncertainties in the tail magnetic field given by the two Tsyganenko models, in model 3 we tried to get better estimates of B_z and $\partial B_{xy}/\partial z$. We computed the equatorial B_z from a force balance formula [*Wolf et al*., 2006, equation (9)] using the observed plasma pressure and magnetic field that were measured in the vicinity of the equatorial plane. The *Wolf* formula is established by relaxing the T96 field to achieve force balance. Note that on the dayside magnetic field lines are not stretched so that B_z does not change much with distance away from the equatorial plane. Thus, the estimated equatorial B_z on the dayside is very close to the observed B_z. We also compare the B_x and B_y computed from the T96 ($B_{xy,\ T96}$) with observed B_x and B_y ($B_{xy,\ observed}$) and modified the $\partial B_{xy}/\partial z$ computed from the T96 ($(\partial B_{xy}/\partial z)_{T96}$) based on the difference so that $\partial B_{xy}/\partial z = (\partial B_{xy}/\partial z)_{T96}$ ($B_{xy,\ observed}/B_{xy,\ T96}$). The estimated K from the three models is shown in Figure 4.

4.1.1. Current Sheet Scattering

[18] Figure 4 shows statistically the distributions of the estimated K as a function of energy at different MLT at the weak and strong *Dst* levels. At a same location, K decreases with increasing ion energy. In the tail plasma sheet, for ions of the same energy, the T96 gives a K almost an order of magnitude smaller than does the model 3 mainly due to the underestimation of B_z by the T96. Model 3 predicts at the weak *Dst* level that at midnight beyond $r = 10\ R_E$, K is <8 for ions above a few hundreds of eV and becomes $\ll 1$ when ion energy is above several hundreds of keV. Thus, ions from a few hundreds of eV to a few hundreds of keV are expected to have chaotic motion and can be isotropized by the current sheet. This energy range has no clear dependence on r in the tail plasma sheet. These are quite consistent with the observations shown in Figure 3a.

[19] At the strong *Dst* level, the predicted energy range for isotropic ions become higher mainly due to higher B_z in the tail plasma sheet, and it can be seen in Figure 3 that the majority of isotropic ions are at higher energy than at the weak *Dst* level. However, Figure 3c shows that isotropic PADs at <0.1 keV ions can be more often seen at stronger *Dst* levels, which cannot be explained by current sheet scattering predicted using a steady magnetic field configuration. However, there is more substorm activity at stronger *Dst* levels, which can generate substantial temporal changes in magnetic field in the tail plasma sheet, including localized current sheet

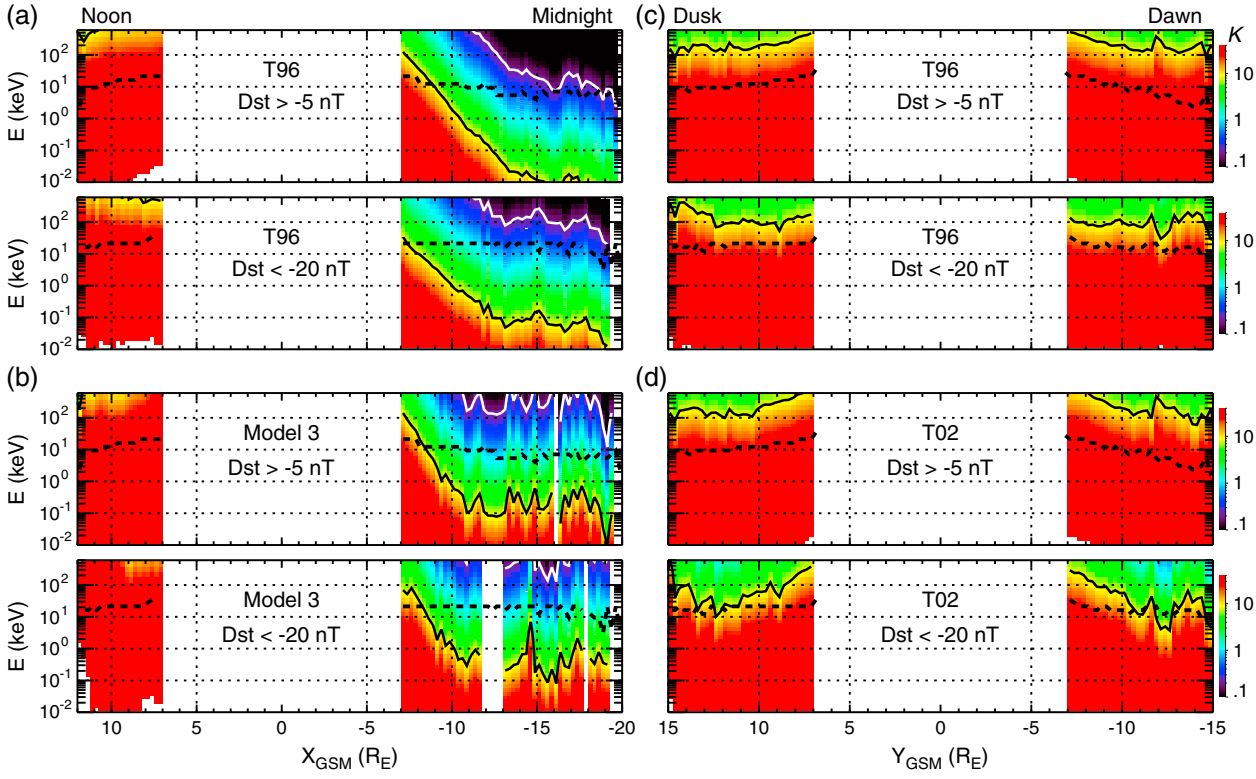

Figure 4. The adiabaticity parameter K versus ion energy at the weak ($Dst > -5$ nT) and strong ($Dst < -20$ nT) Dst level along the noon-midnight meridian estimated using (a) T96 and (b) model 3, and along the dawn-dusk meridian estimated using (c) T96 and (d) T02. The black solid curves indicate $K = 8$ and the white solid curves indicate $K = 0.2$. The black dashed curves indicate ion thermal energies (defined here as the energy of peak ion energy fluxes).

thinning. This may break the adiabaticity of low-energy ions (<0.1 keV) whose motion would be adiabatic under the average empirical magnetic field as indicated by their very large K shown in Figure 4. This could contribute to isotropizing ions at <0.1 keV at stronger Dst levels as shown in Figure 3. Thus, the above results indicate that current sheet scattering is the main process in producing isotropic PADs in the tail plasma sheet where the magnetic field lines are highly stretched.

[20] In the nightside near-Earth magnetosphere, the predicted minimum energy for particles to be isotropized by the current sheet ($K = 8$) increases sharply with decreasing distance from 1 keV at $r = 10$ R_E to ~100 keV at $r = 7$ R_E due to increasing B_z. However, the observations show a much slower increase in the energy ranges of isotropic population. Near the dusk and dawn MLTs, the predicted current sheet scattering can only isotropize ions of energy as low as a 100 keV at the weak Dst level and several tens of keV at the strong Dst level, while isotropic ions are observed at energies much lower than would be expected from current sheet scattering. On the dayside, no ions below at least 600 keV can be isotropized by the current sheet scattering. Therefore, the current sheet scattering cannot isotropize the majority of ions in the near-Earth magnetosphere.

4.1.2. Speiser Motion

[21] As shown in Figure 4, ions of a few hundreds of keV and above in the tail plasma sheet have $K \ll 1$, suggesting they may have Speiser-type motion. The Speiser trajectory [*Speiser*, 1965] includes meandering motion within the magnetic field reversal, as well as particles escaping and returning to the reversal along a more field-aligned direction, resulting a PAD with relatively higher fluxes near 0° or 180° [e.g., *Lyons and Speiser*, 1982; *Ashour-Abdalla et al.*, 1996] in the region outside the reversal. This can account for the negative anisotropy seen at the >~200 keV ions shown in Figures 2 and 3. Figure 5a shows an example of observed two-dimensional distributions of phase space density in the $V_\perp$ and $V_\parallel$ plane when large negative A for 200 keV ions is observed. The enhanced phase space density in the parallel direction above 100 keV shows an ion population well separated from the plasma sheet thermal population. This two-component structure is consistent with simulated PAD by *Ashour-Abdalla et al.* [1996]. As shown in their Plate 11, the simulation shows a PAD consisting of one thermal component and one component at higher energy made up of particles on Speiser-type motion.

[22] In addition to Speiser-type motion, there are many processes accelerating particles preferentially along the field-aligned direction that result in negative anisotropy, such as Fermi acceleration, field-aligned potential drops, or Alfvén waves. Fermi acceleration is effective for particles conserving their second adiabatic invariant, thus it is likely not important in affecting high-energy ions in the tail whose motion is chaotic. It may be effective within bursty bulk flows where magnetic field quickly dipolarizes. Field-aligned potential drops are typically of the order of a few keV [e.g., *Sakanoi*

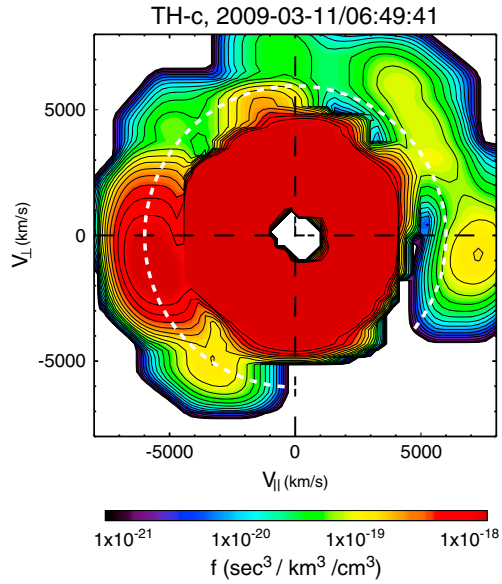

Figure 5. Ion phase space density in the $V_{\perp}$–$V_{||}$ plane observed by THEMIS-C at 06:49:41 UT on 11 March 2009. The white dashed circle indicates 200 keV.

et al., 1995], so they are not expected to accelerate particles to hundreds of keV. Reconnection within the tail plasma sheet may cause sporadic enhanced precipitation of ion from <1 keV to >14 keV [*Sauvaud et al*.,] after substorm expansion onset. The above processes are localized as well as transient, and occur more frequently during more active time. Therefore, compared with Speiser-type motion, they are less likely to be the main cause for the negative anisotropy for ions above hundreds of keV that is seen throughout the tail plasma sheet during weaker *Dst* level.

4.1.3. Adiabatic Motion

[23] As indicated by the estimated K shown in Figure 4, in the near-Earth magnetosphere the majority of ions are expected to conserve their first and second adiabatic invariants as they drift. It has been shown analytically that particles of the same energy but with different pitch angle may follow different drift paths due to MLT-asymmetry of the magnetospheric electric field [e.g., *Roederer and Schulz*, 1971] or magnetic field [e.g., *Roederer*, 1967], which is so-called drift shell splitting. Additionally, the Alfvén layer, which indicates the innermost location a particle can reach along its open drift paths, also depends on pitch angle [e.g., *Kivelson and Southwood*, 1975]. Therefore, in this section, we evaluate if pitch angle dependent drift can qualitatively account for the observed anisotropy in the near-Earth magnetosphere. Note that there have been many inner magnetosphere simulations [e.g., *Jordanova et al*., 1997; *Fok et al*., 1996; *Chen et al*., 1998] that include ion drift conserving the first and second adiabatic invariants using empirical electric and magnetic fields. These simulations can give global distributions of ion anisotropy at different energies and some of these simulation results have been compared with ion anisotropy observed during individual events. However, incorporating one of the above models with conditions appropriate for quantitative comparison with the statistical observations described in section 3 is beyond the scope of this study.

[24] *Kivelson and Southwood* [1975] showed analytically that for low-energy ions dominated by electric drift, the Alfvén layer of field-aligned particles in the morning sector is at smaller r, thus allowing them to penetrate deeper into the inner magnetosphere, compared with particles in the perpendicular direction (the difference is opposite in the evening sector but is much smaller), resulting in a PAD with higher fluxes in the field-aligned direction and negative A. Therefore, this Alfvén layer difference can be one of the processes responsible for the negative A seen in <~1 keV ions in the inner magnetosphere in the postmidnight sector as shown in Figures 2 and 3. As discussed in section 4.2, ionosphere outflow is another important process for producing PADs with negative A for low-energy ions.

[25] The Alfvén layer changes with energy. As ion energy increases, westward magnetic drift can become comparable to eastward electric drift in the morning sector (due to shielding electric field and corotation electric field, the electric drift is dominantly eastward in the morning sector and westward in the evening sector). As a result, the weakened azimuthal drift in the morning sector allows ions to drift more radially to smaller r than ions of lower or higher energies. In addition, 90° pitch angle ions have stronger magnetic drift than particles of other pitch angles. Therefore, ions of 90° pitch angle can go to smaller r than ions of other pitch angles, which result in positive A due to the difference of the Alfvén layers. This could explain the positive A seen in 1 keV ions at the prenoon MLTs, and that this positive A region in the morning sector rotates westward in the morning sector from pre-noon to postmidnight MLTs as energy increases to ~10 keV. Figure 6 shows the radial profiles of the particle fluxes of 5 keV ions at 11° and 78° pitch angle at different MLT at the weak *Dst* level. As shown in Figures 2 and 3, 5 keV ions have strongly positive A around the dawn MLTs inside $r \sim 10\ R_E$. It can be seen from Figure 6 that the fluxes at 11° drop suddenly within the positive A region and become significantly lower than those of 78°. This suggests ions of 11° have little access to this region, as would be expected to observe from crossing their Alfvén layer.

[26] For high-energy ions dominated by magnetic drift, magnetic drift shell splitting is important. For example, *Takahashi et al*. [1997] showed that in a realistic magnetic field configuration (compressed on the dayside and stretched on the nightside) for particles of the same energy at $r = r_0$ at noon, 90° ions come from $r < r_0$ at the midnight MLT while 30° ions come from $r > r_0$. Figure 7 shows the fluxes of 30 keV ions at 78° and 11° at the noon and midnight MLTs. The fluxes increase with decreasing r at midnight and the fluxes at 78° are almost the same as at 11°. Due to magnetic shell splitting and the radial profiles of increasing fluxes with decreasing r on the nightside, 78° ions at noon come from smaller r at midnight, and thus have higher fluxes, than do 11° ions, resulting in a PAD at noon with positive A. At the strong *Dst* level, the radial inward increase on the nightside becomes smaller, thus the difference in the fluxes between 11° and 78° ions at noon becomes smaller too, resulting a PAD with smaller anisotropy.

[27] Due to magnetic drift shell splitting, 90° ions from the nightside at larger r are more likely to hit the duskside magnetopause than are ions of other pitch angles. These particles are lost to the magnetopause and thus cannot complete the drift circle and return back to the nightside. As a result, there

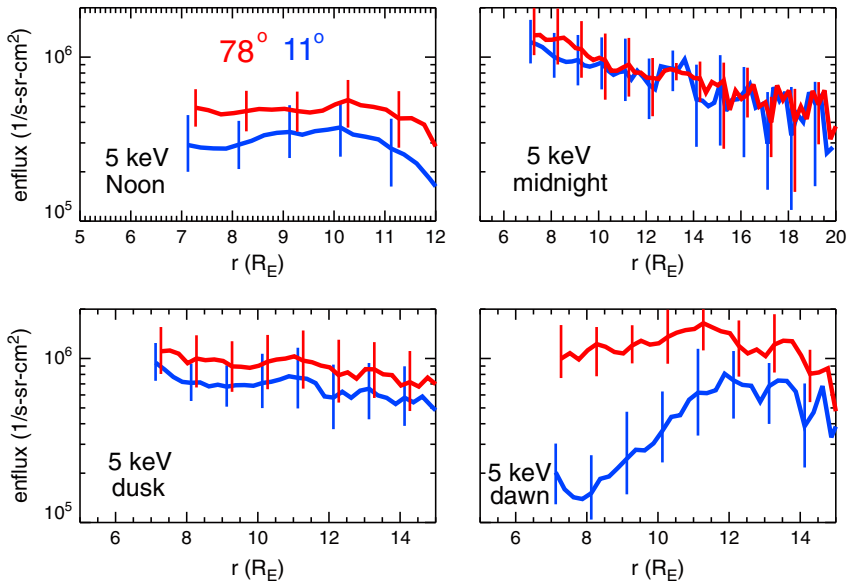

Figure 6. The radial profiles of the energy fluxes of 5 keV ions at 11° (blue) and 78° pitch angles (red) along different MLTs at $Dst > -5$ nT.

are relatively fewer ions near 90° than ions of other pitch angles in the postmidnight sector. This process is known as magnetopause shadowing. Magnetopause shadowing produces butterfly PADs with negative A in the postmidnight sector [e.g., *Sibeck et al.*, 1987; *Fritz et al.*, 2003]. We examined the shape of PADs in the horn-shape negative A region observed at high-energy ions as shown in Figures 2 and 3 and found that the PADs have dominantly a butterfly distribution. Therefore, magnetopause shadowing can account for the horn-shape negative A region observed at high-energy ions.

4.2. Ionospheric Outflow

[28] In the tail plasma sheet, ions below a few hundreds of eV cannot be isotropized by the current sheet scattering as indicated by the estimated K shown in Figure 4. At auroral latitudes, electron precipitation can cause outflow of ions of characteristic energy of a few hundreds of eV [e.g., *Peterson et al.*, 2006], thus enhancing ion fluxes in the field-aligned direction and a PAD with negative A as a result. This can explain the observed negative A for the very low-energy ions from the tail plasma sheet to the near-Earth magnetosphere. During disturbed times, enhanced electron precipitation can cause larger ion outflow fluxes [e.g., *Strangeway et al.*, 2005] and higher outflow energy due to the field-aligned potential drop associated with strong upward field-aligned currents (FACs). The most negative anisotropy of low energy is seen in the midnight-to-dawn MLTs, coinciding with the region of upward FACs of the region-2 FACs, supporting outflow to be one of the processes causing the observed negative A.

[29] To further evaluate the role of ionosphere outflow, we used THEMIS electron energy fluxes to estimate the maximum precipitation energy fluxes assuming strong pitch angle diffusion everywhere for all electron energies. Figure 8a shows that as the estimated electron precipitation energy flux increases in the postmidnight sector, the fluxes of field-aligned low-energy ions increases more than do those along the perpendicular direction, resulting in more strongly negative anisotropy of low-energy ions. Figure 8b shows that A becomes more negative with increasing electron precipitation energy fluxes, consistent with expected higher energy in the ionospheric outflow. These suggest that the ionosphere outflow can be an important contributor to the negative A observed for low-energy ions. Figure 9 shows, for the low-energy ions whose anisotropy is negative, that the difference between the fluxes near 11° and 169° is very small most of the time, which is consistent with the expectation of flux enhancement in both near 0° and 180° pitch angles due to outflow coming from both hemispheres.

4.3. Wave-Particle Interaction

[30] Figures 4 indicates that current sheet scattering is not effective for ions below several hundreds of keV on the dayside. It has been shown in simulations that interaction between ions and EMIC waves can result in pitch angle scattering and precipitation of ions >1 keV [e.g., *Jordanova*

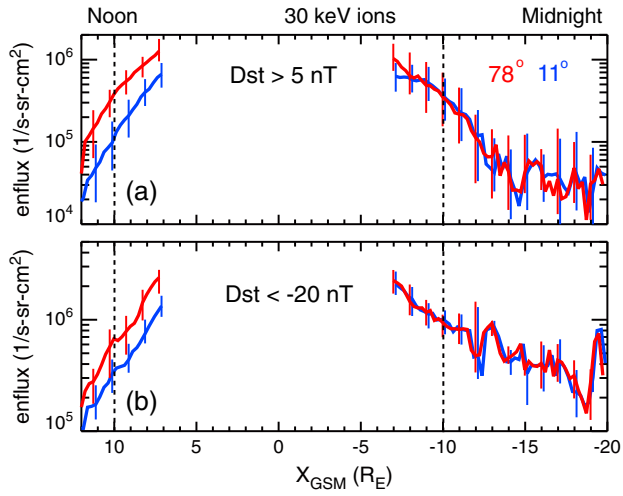

Figure 7. The radial profiles of the energy fluxes of 30 keV ions at 11° (blue) and 78° pitch angles (red) along noon-midnight meridians at (a) $Dst > -5$ nT and (b) $Dst < -20$ nT.

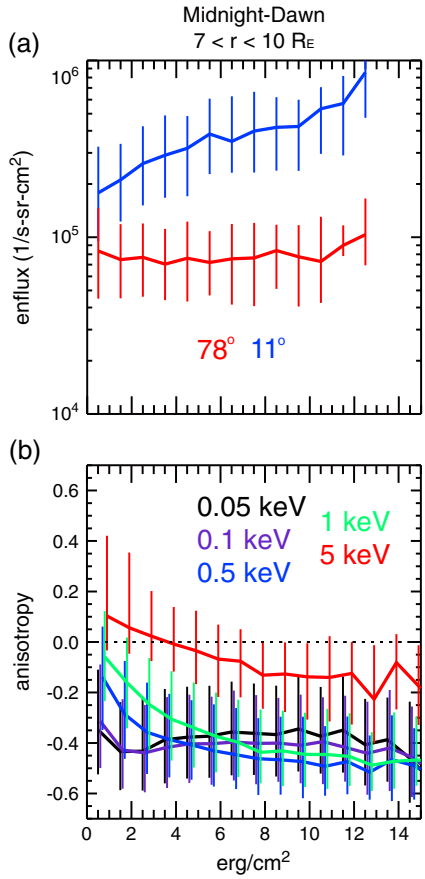

Figure 8. (a) The energy fluxes of 0.5 keV ions at 11° (blue) and 78° pitch angles as a function of estimated maximum precipitation electron energy flux. (b) Anisotropy of ions of different energies as a function of estimated maximum precipitation electron energy flux (from all the data between the midnight to dawn MLTs at $r = 7$ to 10 R_E).

et al., 2001]. The EMIC waves are generated by enhanced positive anisotropy of ions of a few tens of keV (driven by magnetospheric compression or substorm injection); the waves in turn scatter these source ions as well as ions of higher energy (up to a few hundreds of keV) and reduce their anisotropy. A recent study using THEMIS observations [*Usanova et al.*, 2012] shows that magnetospheric compression driven EMIC waves are observed more frequently closer to the dayside magnetopause and during higher solar wind dynamic pressure and lower symmetric disturbance index (SYM), while high occurrence rate for substorm driven EMIC waves is seen preferentially in the afternoon MLTs from ~6 to 13 R_E during high *AE*.

[31] Figures 2 and 3 show that anisotropy of high-energy ions (>~40 keV) drops significantly outside $r \sim 10$ R_E near the dayside magnetopause, which may be due to scattering by the magnetospheric compression driven EMIC waves. To evaluate if there is anisotropy reduction that may be associated with scattering by substorm-driven EMIC waves, we sorted the anisotropy data according to their corresponding *AE* and compute the occurrence rate of isotropic ions ($|A| < 0.1$) for low ($AE < 100$ nT) and high *AE* level ($100 < AE < 500$ nT). Figure 10 shows that for the low *AE* level, ions above ~40 keV on the dayside magnetosphere have a relatively higher isotropy occurrence rate closer to the dayside magnetopause where compressional driven EMIC waves frequently occur. When *AE* is higher, increase of isotropy occurrence rate (thus decrease of anisotropy) on the dayside outside $r \sim 8$ R_E is larger at higher energy (>60 keV) than lower energy (<20 keV), and the increase at high energy is relatively lager near dusk than dawn. The region and *AE* level for higher isotropy occurrence rate is similar to the occurrence rate of substorm-driven EMIC waves, suggesting a positive correlation between these two. However, as discussed in section 4.1.3, decrease of anisotropy on the dayside can be also due to the midnight radial profiles of particle sources becoming flatter, which is also associated with substorm activity. It is likely both processes contribute to the increase of isotropy occurrence rate.

4.4. Ion Losses

[32] In addition to the loss due to magnetopause shadowing described in section 4.1.3, in the inner magnetosphere ions can be lost due to change exchange with the geocorona or Coulomb collisions with the plasmasphere [e.g., *Fok et al.*, 1991]. Both losses are stronger for field-aligned ions than for ions along the perpendicular direction, thus producing a PAD with positive *A*. Nevertheless, the plasmasphere and geocorona are located at small radial distances and we only investigated the region outside $r = 7$ R_E, thus these two losses are not expected to play an important role in affecting the PADs shown in this study.

5. Summary

[33] In this study, we have quantified the pitch angle anisotropy for ions of different energies observed by THEMIS and determined statistically the spatial distributions of anisotropy from the tail plasma sheet to the near-Earth magnetosphere at different *Dst* levels.

[34] In the tail plasma sheet the majority of ions from a few keV to a few tens of keV are isotropic, while the anisotropy for ions below hundreds of eV or above a few hundreds of keV is mainly negative. In the near-Earth magnetosphere, anisotropy varies significantly with MLT. Anisotropy is negative for low-energy ions (< a few hundreds of eV) and is

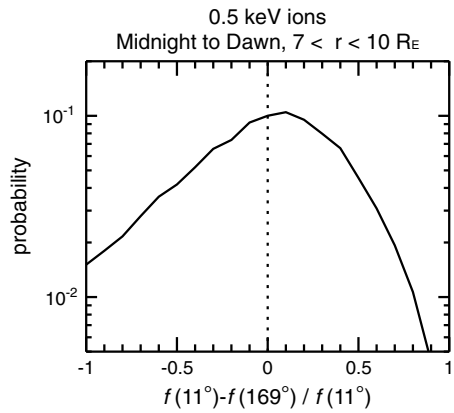

Figure 9. Probability distributions of the difference between the fluxes at 11° and 169° pitch angles for 0.5 keV ions (normalized to the fluxes at 11° pitch angle) from all the data between the midnight to dawn MLTs at $r = 7$ to 10 R_E.

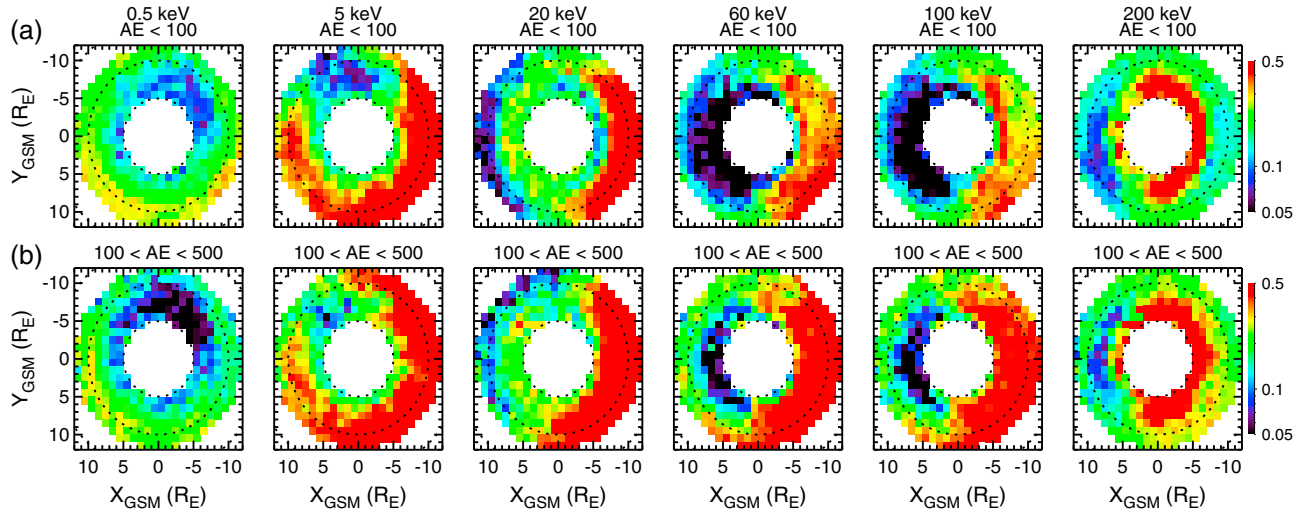

Figure 10. Probability of $|A| \leq 0.1$ at different ion energies at (a) $AE < 100$ nT and (b) $100 < AE < 500$ nT.

strongly negative in the postmidnight sector. Anisotropy becomes positive for ions between ~1 to 10 keV and the region of strongly positive anisotropy rotates westward from the dayside to nightside with increasing ion energy. For ions of ~10 keV and above, positive anisotropy is seen on the dayside centered at noon and negative anisotropy can be seen on the nightside. As the *Dst* level becomes stronger, PADs for ions above 10 keV become less anisotropic for both positive and negative *A*. For ions from 0.1 to several keV, the region of negative *A* extends to larger radial distance at stronger *Dst* levels.

[35] We used different magnetic field models to compute the adiabaticity parameter (*K*) to evaluate likely particle motion at different locations and energies. The results indicate that pitch angle diffusion by the current sheet scattering can be the main process for the observed isotropic ion population from a few keV to a few tens of keV in the tail plasma sheet. The negative anisotropy observed at ions of a few hundreds of keV and above in the tail is likely a result of ions under Speiser motion.

[36] In the near-Earth magnetosphere, the majority of ions are expected to electric and magnetic drift conserving their first and second adiabatic invariants. Drift shell splitting can qualitatively account for the positive anisotropy observed for ions above 1 keV, the MLTs of the positive anisotropy, and the dependence of MLTs on ion energy. For ions above ~30 keV, magnetopause shadowing becomes important; this together with drift shell splitting results in the negative anisotropy seen on the nightside.

[37] For ions below a few hundreds of eV, their PADs can be significantly affected by field-aligned ionosphere outflow and thus have negative anisotropy. The negative anisotropy becomes more negative with increasing electron precipitation energy fluxes estimated from observed equatorial electrons, consistent with increasing contributions from the ionosphere outflow.

[38] Previous simulation results indicate that EMIC waves can be important for scattering high-energy ions. Also, recent THEMIS observations show that EMIC waves on the dayside are more frequently observed at larger *r* and during higher *AE* levels. The occurrence rate of isotropic ions ($|A| < 0.1$) at several tens of keV on the dayside increases with *AE* levels and a larger increase is seen at larger *r*, similar to EMIC occurrence rate. This suggests the important role of EMIC waves in isotropizing high-energy ions on the dayside.

[39] In this study, we examined various processes to evaluate whether they can explain the observed anisotropy. In the future, simulations including all these processes should be conducted and compared with the observations presented here to quantitatively determine the dominant processes responsible for causing the observed anisotropy.

[40] **Acknowledgments.** The work by C.-P. Wang and L. R. Lyons have been supported by NASA grants NNX07AF66G, NNX07AG42G, NNX09AQ41H, and NNX08A135G, and NSF grants ATM-0819864 and ATM-1003595. The work by S. G. Zaharia has been supported by NASA grant NNH09AL06I and NSF grants ATM-0902941 and AGS-1131873. We acknowledge NASA contract NAS5-02099 for THEMIS, and C. W. Carlson and J. P. McFadden for the use of ESA data, D. Larson and R. P. Lin for use of the SST data, K. H. Glassmeier, U. Auster and W. Baumjohann for the use of FGM data provided under DLR contract 50 OC 0302. OMNI data. We thank Drew Turner for useful discussion in processing the SST data. *AE* index was provided by World Data Center for Geomagnetism, Kyoto. We thank the support of ISSI International Teams Program: Plasma Entry and Transport in the Plasma Sheet.

References

Ashour-Abdalla, M., L. A. Frank, W. R. Paterson, V. Peroomian, and L. M. Zelenyi (1996), Proton velocity distributions in the magnetotail: Theory and observations, *J. Geophys. Res.*, *101*(A2), 2587–2598, doi:10.1029/95JA02539.

Baker, D. N., P. R. Higbie, E. W. Hones Jr., and R. D. Belian (1978), High-resolution energetic particle measurements at 6.6 R_E: 3. Low-energy electron anisotropies and short-term substorm predictions, *J. Geophys. Res.*, *83*, 4863–4868.

Burkhart, G. R., and J. Chen (1991), Differential Memory in the Earth's Magnetotail, *J. Geophys. Res.*, *96*(A8), 14,033–14,049, doi:10.1029/91JA01137.

Büchner, J., and L. M. Zelenyi (1989), Regular and chaotic charged particle motion in magnetotaillike field reversals: 1. Basic theory of trapped motion, *J. Geophys. Res.*, *94*(A9), 11,821–11,842, doi:10.1029/JA094iA09p11821.

Chappell, C. R., M. M. Huddleston, T. E. Moore, B. L. Giles, and D. C. Delcourt (2008), Observations of the warm plasma cloak and an explanation of its formation in the magnetosphere, *J. Geophys. Res.*, *113*, A09206, doi:10.1029/2007JA012945.

Chen, M. W., J. L. Roeder, J. F. Fennell, L. R. Lyons, and M. Schulz (1998), Simulations of ring current proton pitch angle distributions, *J. Geophys. Res.*, *103*(A1), 165–178, doi:10.1029/97JA02633.

Delcourt, D. C., J.-A. Sauvaud, R. F. Martin Jr., and T. E. Moore (1996), On the nonadiabatic precipitation of ions from the near-Earth plasma sheet, *J. Geophys. Res.*, *101*(A8), 17,409–17,418, doi:10.1029/96JA01006.

Fennell, J. F., D. R. Croley Jr., and S. M. Kaye (1981), Low-Energy Ion Pitch Angle Distributions in the Outer Magnetosphere: Ion Zipper Distributions, *J. Geophys. Res.*, *86*(A5), 3375–3382, doi:10.1029/JA086iA05p03375.

Fok, M.-C., J. U. Kozyra, A. F. Nagy, and T. E. Cravens (1991), Lifetime of Ring Current Particles Due to Coulomb Collisions in the Plasmasphere, *J. Geophys. Res.*, *96*(A5), 7861–7867, doi:10.1029/90JA02620.

Fok, M.-C., T. E. Moore, and M. E. Greenspan (1996), Ring current development during storm main phase, *J. Geophys. Res.*, *101*(A7), 15,311–15,322, doi:10.1029/96JA01274.

Fritz, T. A., M. Alothman, J. Bhattacharjya, D. L. Matthews, and J. Chen (2003), Butterfly pitch-angle distributions observed by ISEE-1, *Planet. Space Sci.*, *51*, 205–219.

Huang, C.-L., H. E. Spence, H. J. Singer, and N. A. Tsyganenko (2008), A quantitative assessment of empirical magnetic field models at geosynchronous orbit during magnetic storms, *J. Geophys. Res.*, *113*, A04208, doi:10.1029/2007JA012623.

Iglewicz, B., and D. Hoaglin (1993), "Volume 16: How to Detect and Handle Outliers", The ASQC Basic References in Quality Control: Statistical Techniques, Edward F. Mykytka, Ph.D., Editor.

Kivelson, M. G., and D. J. Southwood (1975), Approximations for the Study of Drift Boundaries in the Magnetosphere, *J. Geophys. Res.*, *80*(25), 3528–3534, doi:10.1029/JA080i025p03528.

Jordanova, V. K., J. U. Kozyra, A. F. Nagy, and G. V. Khazanov (1997), Kinetic model of the ring current-atmosphere interactions, *J. Geophys. Res.*, *102*(A7), 14,279–14,291, doi:10.1029/96JA03699.

Jordanova, V. K., C. J. Farrugia, R. M. Thorne, G. V. Khazanov, G. D. Reeves, and M. F. Thomsen (2001), Modeling ring current proton precipitation by electromagnetic ion cyclotron waves during the May 14–16, 1997, storm, *J. Geophys. Res.*, *106*(A1), 7–22, doi:10.1029/2000JA002008.

Lyons, L. R., and T. W. Speiser (1982), Evidence for Current Sheet Acceleration in the Geomagnetic Tail, *J. Geophys. Res.*, *87*(A4), 2276–2286, doi:10.1029/JA087iA04p02276.

McCollough, J. P., J. L. Gannon, D. N. Baker, and M. Gehmeyr (2008), A statistical comparison of commonly used external magnetic field models, *Space Weather*, *6*, S10001, doi:10.1029/2008SW000391.

McFadden, J. P., C. W. Carlson, D. Larson, V. Angelopoulos, M. Ludlam, R. Abiad, B. Elliott, P. Turin, and M. Marckwordt (2008), The THEMIS ESA plasma instrument and in-flight calibration, *Space Sci. Rev*, doi:10.1007/s11214-008-9440-2.

Nagai, T., J. F. E. Johnson, and C. R. Chappell (1983), Low-Energy (<100 eV) Ion Pitch Angle Distributions in the Magnetosphere by ISEE 1, *J. Geophys. Res.*, *88*(A9), 6944–6960, doi:10.1029/JA088iA09p06944.

Peterson, W. K., H. L. Collin, O. W. Lennartsson, and A. W. Yau (2006), Quiet time solar illumination effects on the fluxes and characteristic energies of ionospheric outflow, *J. Geophys. Res.*, *111*, A11S05, doi:10.1029/2005JA011596.

Roederer, J. G. (1967), On the Adiabatic Motion of Energetic Particles in a Model Magnetosphere, *J. Geophys. Res.*, *72*(3), 981–992, doi:10.1029/JZ072i003p00981.

Roederer, J. G., and M. Schulz (1971), Splitting of Drift Shells by the Magnetospheric Electric Field, *J. Geophys. Res.*, *76*(4), 1055–1059, doi:10.1029/JA076i004p01055.

Roederer, J. G., H. H. Hilton, and M. Schulz (1973), Drift Shell Splitting by Internal Geomagnetic Multipoles, *J. Geophys. Res.*, *78*(1), 133–144, doi:10.1029/JA078i001p00133.

Sauvaud, J.-A., D. Popescu, D. C. Delcourt, G. K. Parks, M. Brittnacher, V. Sergeev, R. A. Kovrazhkin, T. Mukai, and S. Kokubun (1999), Sporadic plasma sheet ion injections into the high-altitude auroral bulge: Satellite observations, *J. Geophys. Res.*, *104*(A12), 28,565–28,586, doi:10.1029/1999JA900293.

Sakanoi, T., H. Fukunishi, and T. Mukai (1995), Relationship between field-aligned currents and inverted-V parallel potential drops observed at midaltitudes, *J. Geophys. Res.*, *100*(A10), 19,343–19,360, doi:10.1029/95JA01285.

Sergeev, V. A., E. Sazhina, N. A. Tsyganenko, J. Lundblad, and F. Soraas (1983), Pitch-angle scattering of energetic protons in the magnetotail current sheet as the dominant source of their isotropic precipitation into the nightside ionosphere, *Planet. Space Sci.*, *31*(10), 1147–1155, doi:10.1016/0032-0633(83)90103-4.

Sergeev, V. A., M. Malkov, and K. Mursula (1993), Testing the isotropic boundary algorithm method to evaluate the magnetic field configuration in the tail, *J. Geophys. Res.*, *98*, 7609.

Sibeck, D. G., R. W. McEntire, A. T. Y. Lui, R. E. Lopez, and S. M. Krimigis (1987), Magnetic Field Drift Shell Splitting: Cause of Unusual Dayside Particle Pitch Angle Distributions during Storms and Substorms, *J. Geophys. Res.*, *92*(A12), 13,485–13,497, doi:10.1029/JA092iA12p13485.

Speiser, T. W. (1965), Particle Trajectories in Model Current Sheets 1. Analytical Solutions, *J. Geophys. Res.*, *70*(17), 4219–4226, doi:10.1029/JZ070i017p04219.

Strangeway, R. J., R. E. Ergun, Y.-J. Su, C. W. Carlson, and R. C. Elphic (2005), Factors controlling ionospheric outflows as observed at intermediate altitudes, *J. Geophys. Res.*, *110*, A03221, doi:10.1029/2004JA010829.

Takahashi, K., B. J. Anderson, S. Ohtani, G. D. Reeves, S. Takahashi, T. E. Sarris, and K. Mursula (1997), Drift-shell splitting of energetic ions injected at pseudo-substorm onsets, *J. Geophys. Res.*, *102*(A10), 22,117–22,130, doi:10.1029/97JA01870.

Tsyganenko, N. A. (1995), Modeling the Earth's magnetospheric magnetic field confined within a realistic magnetopause, *J. Geophys. Res.*, *100*, 5599–5612.

Tsyganenko, N. A. (1996), Effects of the solar wind conditions on the global magnetospheric configuration as deduced from data-based field models, in Proceedings of the ICS-3 Conference on Substorms, Eur. Space Agency Spec. Publ. 389, pp. 181–185, Eur. Space Agency, Noordwijk, Netherlands.

Tsyganenko, N. A. (2002a), A model of the near magnetosphere with a dawn-dusk asymmetry 1. Mathematical structure, *J. Geophys. Res.*, *107*, 1179, doi:10.1029/2001JA000219.

Tsyganenko, N. A. (2002b), A model of the near magnetosphere with a dawn-dusk asymmetry 2. Parameterization and fitting to observations, *J. Geophys. Res.*, *107*, 1176, doi:10.1029/2001JA000220.

Usanova, M. E., I. R. Mann, J. Bortnik, L. Shao, and V. Angelopoulos (2012), THEMIS observations of electromagnetic ion cyclotron wave occurrence: Dependence on AE, SYMH, and solar wind dynamic pressure, *J. Geophys. Res.*, *117*, A10218, doi:10.1029/2012JA018049.

Walsh, A. P., C. J. Owen, A. N. Fazakerley, C. Forsyth, and I. Dandouras (2011), Average magnetotail electron and proton pitch angle distributions from Cluster PEACE and CIS observations, *Geophys. Res. Lett.*, *38*, L06103, doi:10.1029/2011GL046770.

Wang, C.-P., M. Gkioulidou, L. R. Lyons, R. A. Wolf, V. Angelopoulos, T. Nagai, J. M. Weygand, and A. T. Y. Lui (2011), Spatial distributions of ions and electrons from the plasma sheet to the inner magnetosphere: Comparisons between THEMIS-Geotail statistical results and the Rice convection model, *J. Geophys. Res.*, *116*, A11216, doi:10.1029/2011JA016809.

West, H. J., R. M. Buck, and J. R. Walton (1973), Electron pitch angle distributions throughout the magnetosphere as observed on OGO-5, *J. Geophys. Res.*, *78*, 1064–1081.

Wolf, R. A., V. Kumar, F. R. Toffoletto, G. M. Erickson, A. M. Savoie, C. X. Chen, and C. L. Lemon (2006), Estimating local plasma sheet PV5/3 from single-spacecraft measurements, *J. Geophys. Res.*, *111*, A12218, doi:10.1029/2006JA012010.

Young, S. L., R. E. Denton, B. J. Anderson, and M. K. Hudson (2002), Empirical model for μ scattering caused by field line curvature in a realistic magnetosphere, *J. Geophys. Res.*, *107*(A6), 1069, doi:10.1029/2000JA000294.

Zhang, Q.-H., M. W. Dunlop, R. Holme, and E. E. Woodfield (2010), Comparison of eight years magnetic field data from Cluster with Tsyganenko models in the inner magnetosphere, *Ann. Geophys.*, *28*, 309–326, doi:10.5194/angeo-28-309-2010.